

Theoretical Analysis of Open Spherical Microphone Arrays for Acoustic Intensity Measurements

Hüseyin Hacıhabiboğlu*, *Senior Member, IEEE*

Abstract—Acoustic intensity is a vectorial measure of acoustic energy flow through a given region of interest. Three dimensional measurement of acoustic intensity requires special microphone array configurations. This article provides a theoretical analysis of open spherical microphone arrays for the 3-D measurement of acoustic intensity. The calculation of the pressure and the particle velocity components of the sound field inside a closed volume is expressed using the Kirchhoff-Helmholtz integral equation. The conditions which simplify the calculation are identified. This calculation is then constrained to a finite set of microphones positioned at prescribed points on a sphere. Several open spherical array topologies are proposed. Their magnitude and directional errors and measurement bandwidths are investigated via numerical simulations. A comparison with conventional open-sphere 3-D intensity probes is presented.

Index Terms—Microphone arrays, acoustic intensity, spherical arrays, source localization

I. INTRODUCTION

ACOUSTIC intensity represents the net flow of acoustic energy through a given region [1]. It is a physical vector quantity showing the direction and the strength of a sound field at a given measurement position. Instantaneous acoustic intensity at a point \mathbf{x} is defined as:

$$\mathbf{I}(\mathbf{x}, t) = p(\mathbf{x}, t)\mathbf{v}(\mathbf{x}, t) \quad (1)$$

where $p(\mathbf{x}, t)$ is the pressure and $\mathbf{v}(\mathbf{x}, t)$ is the particle velocity vector at that point.

Acoustic intensity has both active and reactive parts. Active intensity refers to the part of the signal energy which *flows*, and reactive intensity refers to the part of the signal energy which is *stored*. The active part of the acoustic intensity is in phase while the reactive part is out of phase with the pressure measured at the same position. For a monochromatic sound field with the angular frequency of $\omega = 2\pi f$, the active and the reactive intensities are defined respectively as [2]:

$$\mathbf{I}_a(\mathbf{x}, \omega) = \frac{1}{2} \Re\{p(\mathbf{x}, \omega)\mathbf{v}^*(\mathbf{x}, \omega)\} \quad (2)$$

$$\mathbf{I}_r(\mathbf{x}, \omega) = \frac{1}{2} \Im\{p(\mathbf{x}, \omega)\mathbf{v}^*(\mathbf{x}, \omega)\} \quad (3)$$

Manuscript received January 25, 2013, revised July 20, 2013, accepted November 19, 2013. The associate editor coordinating the review of this manuscript and approving it for publication was Professor Søren Holdt Jensen. This work was supported by the Middle East Technical University Faculty Research Grant, “BAP-08-11-2013-057 – Sound source localization using open spherical acoustic intensity probes”.

H. Hacıhabiboğlu is with Department of Modelling and Simulation, Graduate School of Informatics, Middle East Technical University, Ankara, Turkey. (e-mail: hhuseyin@metu.edu.tr).

Digital Object Identifier 10.1109/TASL.2013.XXXXXX

where $(\cdot)^*$ denotes complex conjugation.

The pressure and the particle velocity signals are in phase and the reactive intensity is zero for the sound field due to an ideal plane wave propagating in the acoustic free-field. This corresponds to a purely active acoustic intensity. On the other extreme, the non-propagating energy is much stronger in the close vicinity of the sound source. This region, also known as the *acoustic near field*, depends on the frequency and the distance from the source and has a predominantly reactive acoustic intensity [3]. Actual sound fields in real rooms that consist of a combination of direct sound, interference of reflections and diffuse reverberation are neither purely active, nor purely reactive, but have both components.

Apart from its primary use in measuring the acoustic power and the sound radiation [1], active intensity has also been used as a basis for sound source localization [4][5][6], source separation [7][8][9] and spatial audio coding [10][11]. These tasks require the accurate measurement of acoustic intensity.

Active intensity can be measured using two different methods called the *p-p* and the *p-u* methods [12][13]. The *p-p* method uses the sum and difference of signals from two closely positioned pressure probes to obtain finite difference approximations of the pressure and the particle velocity, respectively. Active intensity is then calculated in the axial direction of the microphones at their mid-point. The *p-u* method uses a velocity probe in addition to a pressure probe to avoid systematic errors due to finite difference approximation. A major disadvantage of both methods is their inability to measure 3-D intensity vectors.

Alongside the newer generation micromachined 3-D intensity probes using individual pressure and particle velocity sensors [14][15] there also exist more conventional 3-D vector probes consisting of several *p-p* pairs. These probes typically have either tetrahedral or cubic topology [16][17][18], which are both different sampling schemes on an open sphere.

Several issues with three-dimensional acoustic intensity measurements can be listed. Firstly, the finite number of microphones used in a 3-D intensity probe causes the measurement accuracy to depend on the directions of the sound sources [7]. Secondly, the measurement of intensity in the acoustic near-field or more generally in sound fields with non-negligible reactive components can be problematic [19]. Thirdly, the separation between individual elements used in the design limits the accuracy of the measurements especially at high frequencies due to systematic errors [20]. Finally, the phase mismatches between individual array elements cause errors reducing the accuracy of the arrays at low frequencies [19].

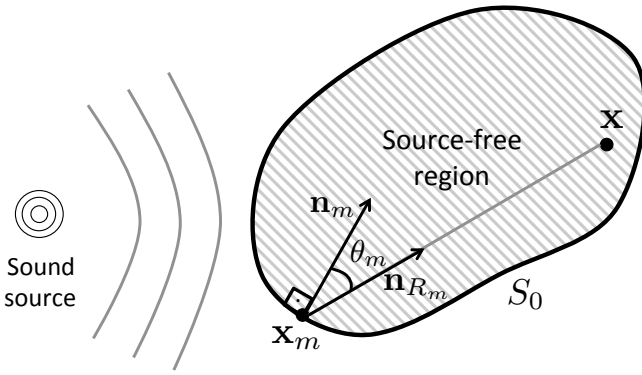


Fig. 1. Geometry of a source-free volume bounded by a surface on which the pressure and the particle velocity due to an external source are known.

A theoretical analysis of open spherical microphone arrays to measure acoustic intensity is presented in this article. Nine open spherical microphone arrays based on the Kirchhoff-Helmholtz integral are proposed. Numerical simulations are provided to demonstrate the accuracy of these arrays for the far-field and the near-field conditions. The effects of array size and component mismatch on the accuracy of the proposed arrays are also investigated. It is shown that the proposed arrays provide a significantly greater measurement bandwidth than the conventional arrays.

This paper is organized as follows. Sec. II discusses the calculation of the intensity based on the Kirchhoff-Helmholtz integral on an open spherical surface. Sec. III presents three quadrature schemes and corresponding array topologies for the numerical calculation of acoustic intensity at the center of the sphere. Sec. III provides a numerical comparison of these array topologies with respect to their ideal response for point sources in the acoustic far-field and near-field. Dependence of the array performance on the array size is evaluated. Errors due to phase mismatches between the array elements are numerically investigated and the proposed arrays are compared with conventional arrays for their performance in monochromatic plane wave fields. Sec. V summarizes the findings and concludes the article.

II. PRESSURE AND VELOCITY AT THE CENTER OF AN OPEN SPHERE

A. Kirchhoff-Helmholtz integral equation

Let us consider a source-free open volume bounded by the surface S_0 as shown in Fig. 1. If the pressure, $p(\mathbf{x}_m, \omega)$, and the particle velocity normal to the surface, $\bar{v}_n(\mathbf{x}_m, \omega)$ at each point $\mathbf{x}_m \in S_0$ are known, the pressure field within the volume enclosed by this surface can be exactly determined using the Kirchhoff-Helmholtz integral equation [21][22]:

$$p(\mathbf{x}, \omega) = \iint_{S_0} \left[j\omega\rho_0\bar{v}_n(\mathbf{x}_m, \omega)G(\mathbf{x}_m|\mathbf{x}, \omega) + p(\mathbf{x}_m, \omega)\frac{\partial G(\mathbf{x}_m|\mathbf{x}, \omega)}{\partial \mathbf{n}_m} \right] dS_0 \quad (4)$$

where,

$$G(\mathbf{x}_m|\mathbf{x}, \omega) = \frac{e^{-jk\|\mathbf{x}-\mathbf{x}_m\|}}{4\pi\|\mathbf{x}-\mathbf{x}_m\|} \quad (5)$$

is the free-field Green's function for a point source, $\omega = 2\pi f$ is the angular frequency, $k = |\omega/c|$ is the wave number, ρ_0 is the air density, \mathbf{n}_m is the unit vector normal to the surface at the point \mathbf{x}_m , and the directional derivative of an arbitrary spatial function $f(\mathbf{x})$ is given as:

$$\frac{\partial f(\mathbf{x})}{\partial \mathbf{n}} = \nabla f(\mathbf{x}) \cdot \mathbf{n}. \quad (6)$$

Euler's equation relates gradient of the pressure field to the time derivative of the particle velocity field such that:

$$\rho_0 \frac{\partial \mathbf{v}(\mathbf{x}, t)}{\partial t} = -\nabla p(\mathbf{x}, t). \quad (7)$$

If Euler's equation is expressed in the frequency domain as $-j\omega\rho_0\mathbf{v}(\mathbf{x}, \omega) = \nabla p(\mathbf{x}, \omega)$, the Kirchhoff-Helmholtz integral can be expressed as a function of the pressure field only:

$$p(\mathbf{x}, \omega) = - \iint_{S_0} \left[\frac{\partial p(\mathbf{x}_m, \omega)}{\partial \mathbf{n}_m} G(\mathbf{x}_m|\mathbf{x}, \omega) - p(\mathbf{x}_m, \omega) \frac{\partial G(\mathbf{x}_m|\mathbf{x}, \omega)}{\partial \mathbf{n}_m} \right] dS_0. \quad (8)$$

The particle velocity is then given as:

$$\mathbf{v}(\mathbf{x}, \omega) = \frac{1}{j\omega\rho_0} \iint_{S_0} \left[\frac{\partial p(\mathbf{x}_m, \omega)}{\partial \mathbf{n}_m} \nabla G(\mathbf{x}_m|\mathbf{x}, \omega) - p(\mathbf{x}_m, \omega) \nabla (\nabla G(\mathbf{x}_m|\mathbf{x}, \omega) \cdot \mathbf{n}_m) \right] dS_0. \quad (9)$$

Defining the unit vector from the point on the surface in the direction of the estimation point, \mathbf{x} , as $\mathbf{n}_{R_m} = (\mathbf{x} - \mathbf{x}_m) / \|\mathbf{x} - \mathbf{x}_m\|$, the following expressions can be given:

$$\nabla G(\mathbf{x}_m|\mathbf{x}, \omega) = - \left(jk + \frac{1}{R_m} \right) G(\mathbf{x}_m|\mathbf{x}, \omega) \mathbf{n}_{R_m}, \quad (10)$$

$$\begin{aligned} \nabla (\nabla G(\mathbf{x}_m|\mathbf{x}, \omega) \cdot \mathbf{n}_m) = & \left(\frac{2}{R_m^2} + \frac{j2k}{R_m} - k^2 \right) G(\mathbf{x}_m|\mathbf{x}, \omega) \langle \mathbf{n}_{R_m}, \mathbf{n}_m \rangle \mathbf{n}_{R_m} \\ & - \left(jk + \frac{1}{R_m} \right) G(\mathbf{x}_m|\mathbf{x}, \omega) \nabla \langle \mathbf{n}_{R_m}, \mathbf{n}_m \rangle, \end{aligned} \quad (11)$$

where $R_m = \|\mathbf{x} - \mathbf{x}_m\|$ and $\langle \bar{\mathbf{n}}_{R_m}, \bar{\mathbf{n}}_m \rangle = \cos \theta_m$ is the inner product of two unit vectors. Note that for the general case the unit vectors, $\bar{\mathbf{n}}_{R_m}$ and $\bar{\mathbf{n}}_m$ are not coincident.

B. Open spherical microphone arrays

The derivation given above did not make any distinction on the shape of the volume and the integration surface. Since we are interested in measuring the acoustic intensity at a single point, positioning individual microphones on an open sphere is a reasonable choice as it allows some useful simplifications.

Let us now consider an open sphere of radius R centered around the coordinate origin (i.e. $\mathbf{x} = 0$). The inward normal unit vector, \mathbf{n}_m , and the unit vector in the direction of the center, \mathbf{n}_{R_m} , are coincident. Therefore, $\nabla \langle \mathbf{n}_{R_m}, \mathbf{n}_m \rangle = 0$ in (11). Also, since each point on the sphere, \mathbf{x}_m , is equidistant from the center, the free-field Green's function between a point positioned on the spherical surface and its center can be simplified to [23]:

$$G(\mathbf{x}_m|0, \omega) = \frac{e^{-jkR}}{4\pi R} \quad (12)$$

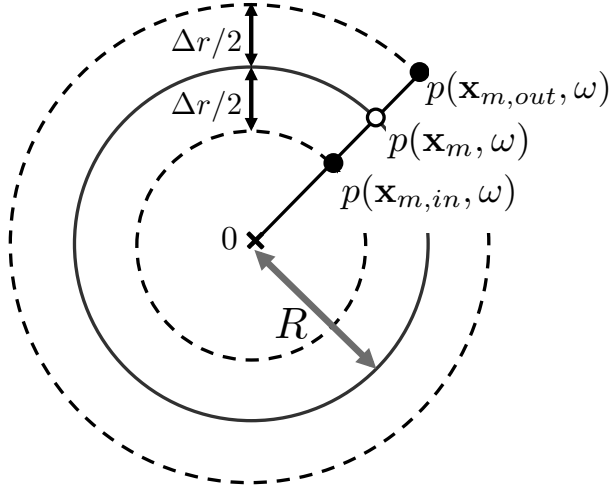


Fig. 2. Calculation of the pressure and the pressure gradient on a measurement surface (solid line) using known pressure distributions on two concentric open surfaces (dashed lines).

where $R = \|\mathbf{x}_m\|$.

A particle velocity probe and a pressure probe cannot be strictly coincident. Therefore, the direct calculation of the Kirchhoff-Helmholtz integral in (4) is not feasible. However, pairs of omnidirectional microphones can be used to approximate both the pressure and the directional derivative of the pressure at a given point.

In order to address this practical limitation, let us assume that the pressure distributions on two concentric open spherical surfaces separated by a radial distance of Δr are known (see Fig. 2). Let us also consider two radially aligned points, $\mathbf{x}_{m,out}$ and $\mathbf{x}_{m,in}$ in the outer and the inner surfaces, respectively:

$$\mathbf{x}_{m,out} = \mathbf{x}_m - \frac{\Delta r}{2} \mathbf{n}_m \quad (13)$$

$$\mathbf{x}_{m,in} = \mathbf{x}_m + \frac{\Delta r}{2} \mathbf{n}_m \quad (14)$$

Given that the pressure signals at these points are known, finite difference approximations to the pressure and the directional derivative of pressure at the point \mathbf{x}_m on another open spherical surface midway between the outer and the inner surfaces can be obtained such that:

$$p(\mathbf{x}_m, \omega) \approx \frac{1}{2} [p(\mathbf{x}_{m,out}, \omega) + p(\mathbf{x}_{m,in}, \omega)] \quad (15)$$

$$\left. \frac{\partial p(\mathbf{x}, \omega)}{\partial \mathbf{n}} \right|_{\mathbf{x}=\mathbf{x}_m} \approx \frac{1}{\Delta r} [p(\mathbf{x}_{m,out}, \omega) - p(\mathbf{x}_{m,in}, \omega)]. \quad (16)$$

Here, a good approximation is obtained if $\Delta r \ll \frac{\lambda}{4}$ where $\lambda = c/f$ is the wavelength. This allows expressing the pressure and the particle velocity at the center as a function of the

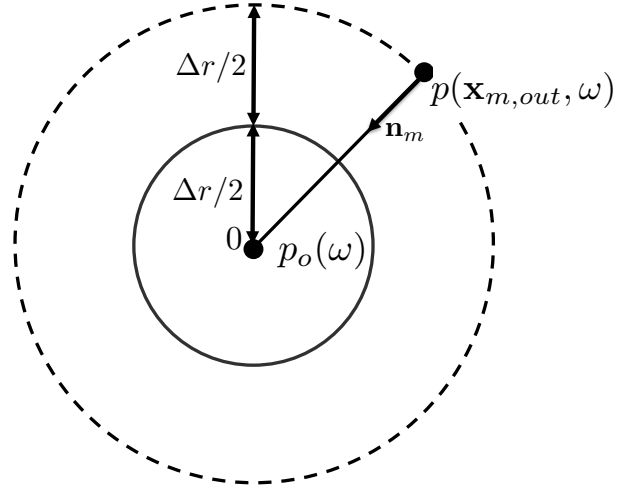


Fig. 3. Open spherical surface with a known pressure distribution (dashed line) and at the center. The particle velocity and the pressure are calculated on the measurement surface (solid line).

pressure distributions on two concentric spherical surfaces:

$$p_o(\omega) = \quad (17)$$

$$-\frac{e^{-jkR}}{4\pi R} \left[\iint_{S_0} \left(\frac{jk}{2} + \frac{1}{2R} + \frac{1}{\Delta r} \right) p(\mathbf{x}_{m,out}, \omega) dS_0 + \iint_{S_0} \left(\frac{jk}{2} + \frac{1}{2R} - \frac{1}{\Delta r} \right) p(\mathbf{x}_{m,in}, \omega) dS_0 \right],$$

$$\mathbf{v}_o(\omega) = -\frac{1}{j\omega\rho_0} \frac{e^{-jkR}}{4\pi R} \times \quad (18)$$

$$\left[\iint_{S_0} \left(\frac{jk}{\Delta r} + \frac{1}{\Delta r R} + \frac{1}{R^2} + \frac{jk}{R} - \frac{k^2}{2} \right) p(\mathbf{x}_{m,out}, \omega) \mathbf{n}_m dS_0 + \iint_{S_0} \left(-\frac{jk}{\Delta r} - \frac{1}{\Delta r R} + \frac{1}{R^2} + \frac{jk}{R} - \frac{k^2}{2} \right) p(\mathbf{x}_{m,in}, \omega) \mathbf{n}_m dS_0 \right].$$

Another useful simplification is possible if the pressure at the center and the pressure distribution on an open spherical surface of radius Δr are known (see Fig. 3). In other words $\mathbf{x}_{m,in} = 0$ and $\mathbf{x}_{m,out} = -\Delta r \mathbf{n}_m$. This allows the calculation of the directional derivative in the radial direction at a radius of $R = \Delta r/2$. Since, the actual pressure at the center is already available, the calculation of (17) becomes unnecessary. Also, the second surface integral in (18) vanishes and the particle velocity can be expressed as:

$$\mathbf{v}_o(\omega) = \quad (19)$$

$$-\frac{1}{j\omega\rho_0} \left(\frac{3}{2R^2} + \frac{j3k}{2R} - \frac{k^2}{2} \right) \frac{e^{-jkR}}{4\pi R} \iint_{S_0} p(\mathbf{x}_{m,out}, \omega) \mathbf{n}_m dS_0.$$

Denoting the pressure signal $p(\mathbf{x}_{m,out}, \omega)$ in the spherical coordinates as $p(\theta, \phi, \omega)$ where $\theta \in [0, \pi]$ and $\phi \in [0, 2\pi)$ are the elevation and azimuth angles, respectively and the area element as $dS_0 = R^2 \sin \theta d\theta d\phi$, the expression given in (19) simplifies to:

$$\mathbf{v}_o(\omega) = \frac{1}{4\pi} F(R, \omega) \int_0^{2\pi} \int_0^\pi p(\theta, \phi, \omega) \mathbf{n}_{\theta, \phi} \sin \theta d\theta d\phi, \quad (20)$$

where $F(R, \omega) = -\frac{1}{j2\omega\rho_0} \frac{e^{-jkR}}{R} (3 + j3kR - k^2R^2)$. This expression corresponds to a parallel combination of an integrator, a gain element and a differentiator in series with a linear phase shift.

III. MICROPHONE ARRAY TOPOLOGIES

Calculation of the acoustic intensity at a given point requires that the pressure and the particle velocity at that point are known. It is assumed in this article that the pressure at the center of the open sphere is directly measured. In order to calculate the exact particle velocity, the pressure has to be known everywhere on the open sphere so that the surface integral given in (20) can be calculated. This is not a feasible requirement. Instead, the pressure distribution on the surface can be sampled at a finite number of points to obtain a bandlimited approximation of the particle velocity. In practice, sampling is done by positioning pressure microphones at those points.

There are several quadrature schemes for obtaining an approximation to a surface integral on a sphere. Three such schemes are summarized and their applicability to the open spherical microphone arrays is discussed in this section. The aim is to express the particle velocity in the following form:

$$\tilde{\mathbf{v}}_o(\omega) = C_s F(R, \omega) \sum_{m=1}^M w_m p(\theta_m, \phi_m, \omega) \mathbf{n}_m \quad (21)$$

where C_s is a constant, and $\{w_m\}$ are the real weights of the respective quadrature schemes. In the following, $C_s = 1$ for the Lebedev quadrature, $C_s = 1/4M$ for the product Gauss quadrature, and $C_s = 1/4\pi$ for the finite element quadrature.

The discussion in this section is limited to a total element count of up to 32 microphones. In the following, the pressure microphone at the center of the array is always implied and when an M -element array is mentioned, the total number of microphones including the pressure microphone at the array center is $M + 1$.

A. Lebedev Quadrature

The Lebedev quadrature scheme allows obtaining an approximation to the integration of a smooth function on a spherical surface. The approximation is accurate up to a given order of spherical harmonics. The Lebedev quadrature uses discrete points with octahedral symmetry on the unit sphere at which individual elements of the microphone array are positioned. The sampling points on the sphere, (θ_m, ϕ_m) are calculated as the vertices of rotational permutations of octahedrons. The approximation to (20) can be obtained by:

$$\tilde{\mathbf{v}}_o(\omega) = F(R, \omega) \sum_{m=1}^M w_m p(\theta_m, \phi_m, \omega) \mathbf{n}_m. \quad (22)$$

Based on the premise that only the array topologies with at most 32 elements are considered, the following numerical

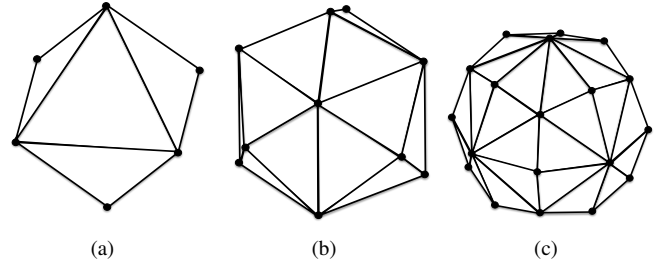


Fig. 4. Microphone array topologies with (a) 6 (octahedron), (b) 14, and (c) 26 elements for use with the first-, second-, and third-order Lebedev quadrature schemes, respectively. The filled black circles show the microphone positions.

scheme holds:

$$\tilde{\mathbf{v}}_o(\omega) = F(R, \omega) \left[A_1 \sum_{m=1}^6 p(\theta_{m,1}, \phi_{m,1}, \omega) \mathbf{n}_{m,1} + A_2 \sum_{m=1}^8 p(\theta_{m,2}, \phi_{m,2}, \omega) \mathbf{n}_{m,2} + A_3 \sum_{m=1}^{12} p(\theta_{m,3}, \phi_{m,3}, \omega) \mathbf{n}_{m,3} \right]. \quad (23)$$

Here, A_1 , A_2 , and A_3 are the first-, second-, and third-order Lebedev grid weights [24]. With the given constraint on the maximum number of microphones, the Lebedev quadrature requires 6, 14, or 26 sampling points on the unit sphere for the approximation of the surface integral up to first-, second-, and third-order spherical harmonics, respectively. Higher order Lebedev grids require more than 32 elements and are thus not considered in this article. Fig. 4 shows the sampling points on the sphere that can be used with the Lebedev quadrature scheme.

B. Product Gauss Quadrature

A numerical approximation to the surface integral in (20) can also be obtained using the product Gauss quadrature [25]. This allows expressing the surface integral as a finite double series:

$$\tilde{\mathbf{v}}_o(\omega) = \frac{1}{4M} F(R, \omega) \sum_{m=1}^{2M} \sum_{n=1}^M w_n p(\theta_n, \phi_m, \omega) \mathbf{n}_{nm}. \quad (24)$$

If the elevation angles, $\{\theta_n\}$ are selected in such a way that $\{\cos \theta_n\}$ are the Gauss-Legendre nodes and $\{w_n\}$ are the corresponding weights on $[-1, 1]$, the discrete sum provides a polynomial approximation of degree $2M$ to the surface integral. The $2M$ azimuth angles are uniformly distributed from 0 to 2π . The total number of measurement points (i.e. microphones) that need to be used with the product Gauss quadrature for an order of M is $2M^2$. The highest order that is discussed in this work is $M = 4$ which corresponds to 32 microphones. Fig. 5 shows the sampling points for product Gauss quadrature on the unit sphere for second, third, and fourth orders corresponding to 8, 18, and 32 array elements, respectively.

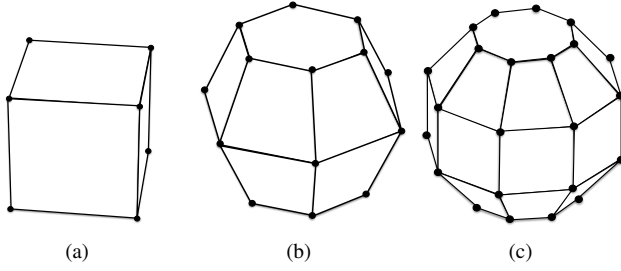


Fig. 5. Microphone array topologies with (a) 8 (cube), (b) 18, and (c) 32 elements for use with the first-, second-, and third-order product Gauss quadrature schemes, respectively. The filled black circles show the microphone positions.

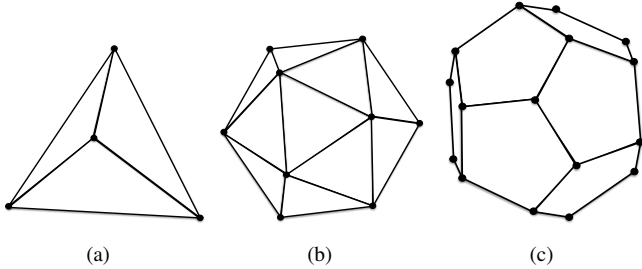


Fig. 6. Microphone array topologies with (a) 4 (tetrahedron), (b) 12 (icosahedron), and (c) 20 (dodecahedron) elements for use with the finite element quadrature scheme. The filled black circles show the microphone positions.

C. Finite Element Quadrature

If the spherical surface is partitioned into a finite number of surface elements, the more straightforward method of centroid rule [25] can be applied. Assuming that $\{\Delta_0, \Delta_1, \dots, \Delta_{n-1}\}$ is a partitioning of the sphere and (θ_m, ϕ_m) is the centroid of Δ_m , a numerical approximation to (20) can be calculated as:

$$\tilde{\mathbf{v}}_o(\omega) \approx \frac{1}{4\pi} F(R, \omega) \sum_{m=0}^{n-1} p(\theta_m, \phi_m, \omega) \mathbf{n}_m A(\Delta_m) \quad (25)$$

where $A(\Delta_m)$ represents the area of the corresponding partition.

While the finite element quadrature allows any partitioning of the spherical surface, only the uniform sampling schemes are considered in this article. Five such choices are the tetrahedral, octahedral, cubic, icosahedral, and dodecahedral topologies, which correspond to 4, 6, 8, 12, and 20 discrete measurement points. Only the topologies with 4, 12, and 20 elements are shown in Fig. 6 as the finite element quadratures for 6 and 8 element arrays are equivalent to the first-order Lebedev quadrature and the second-order product Gauss quadrature, respectively.

IV. COMPARISON OF DIFFERENT SCHEMES AND ARRAY TOPOLOGIES

A numerical comparison of different array topologies is given in this section. Calculation of the acoustic intensity for monochromatic sources is discussed first, followed by the performance metrics used for assessing the arrays. Numerical

simulations that are used to compare different array topologies are then presented.

A. Monochromatic sound fields

Let us assume that we have a steady state monochromatic acoustic field with a frequency of $f_s = 1/T$. The time averaged complex acoustic intensity at a given point can be calculated as:

$$\overline{\mathbf{I}_c(t)} = \frac{1}{2T} \int_0^T p_o(t) \mathbf{v}_o^*(t) dt \quad (26)$$

The time averaged active intensity can be expressed in the frequency domain as:

$$\overline{\mathbf{I}_a(\omega)} = \frac{1}{2} \Re \{ p_o(\omega) \mathbf{v}_o^*(\omega) \}. \quad (27)$$

The time averaged active intensity obtained using the proposed arrays can then be expressed by substituting (21) into (27) such that:

$$\overline{\mathbf{I}_o(\omega)} = \frac{1}{2} \Re \left\{ p_o(\omega) C_s F^*(R, \omega) \sum_{m=1}^M w_m p^*(\theta_m, \phi_m, \omega) \mathbf{n}_m \right\}. \quad (28)$$

B. Performance metrics

Four performance metrics are used to assess different array topologies. In order to compare the performance of the arrays numerically, the *actual* acoustic intensity, $\overline{\mathbf{I}_a(\omega)}$, and the *predicted* acoustic intensity, $\overline{\mathbf{I}_o(\omega)}$ are used.

1) *Directional error*: For certain applications like sound source localization, source separation, and spatial audio coding, the directional accuracy of an array can be more important than its magnitude accuracy. Directional accuracy is assessed by the angle between the actual and the predicted (i.e. measured) time-averaged intensity vectors. This angle can be obtained using the inner product of the actual and the predicted intensity vectors such that:

$$\psi(\omega) = \arccos \frac{\langle \overline{\mathbf{I}_o(\omega)}, \overline{\mathbf{I}_a(\omega)} \rangle}{\|\overline{\mathbf{I}_a(\omega)}\| \|\overline{\mathbf{I}_o(\omega)}\|} \quad (29)$$

If the actual and the predicted intensity vectors are coincident, the angle between them is zero (i.e. $\psi(\omega) = 0$).

2) *Magnitude error*: For applications with the specific purpose of measuring sound power [26], magnitude of the predicted intensity vector is also important. The difference of the norms of the actual and the predicted intensity vectors can be used as a measure of magnitude accuracy. The magnitude error (in dB) is thus defined as:

$$\epsilon(\omega) = 10 \log_{10} \left| \frac{\|\overline{\mathbf{I}_a(\omega)}\| - \|\overline{\mathbf{I}_o(\omega)}\|}{\|\overline{\mathbf{I}_a(\omega)}\|} \right|. \quad (30)$$

3) *Isotropic operating range*: Isotropic operating range, f_{IOR} , is defined as the maximum frequency below which the magnitude error and the directional error are both less than prescribed values. This frequency determines the upper bound at which a uniformly accurate prediction of acoustic intensity can be obtained. The isotropic operating range is thus defined as the maximum frequency at which $\epsilon(\omega) \leq -10$ dB corresponding to a 10% magnitude error and $\psi(\omega) \leq 1^\circ$ for all directions. Different definitions for different purposes are possible. Note that isotropic operating range is defined only for ideal arrays with perfectly matched components. The actual frequency band for which an imperfectly matched array is bounded at both a low and a high frequency.

4) *Measurement bandwidth*: Microphones, even with manufacturer guaranteed tolerances are known to have substantial phase response mismatches [27]. It is assumed that most of these mismatches can be digitally equalized, albeit with small remaining discrepancies [28]. Even then, the phase mismatches of the individual array components are an important source of error [29][30]. These errors decrease the measurement accuracy at low frequencies, and also depend on the array size [13]. While simple solutions such as switching or rotating a p - p probe and using the cross-spectrum of the obtained signals [31] were previously proposed, they are neither directly nor straightforwardly applicable to spherical arrays discussed in this article.

Effects of component mismatches can be investigated using the *direction averaged error norm* defined as:

$$\chi(\theta, \phi, \omega) = 10 \log_{10} \left[\frac{1}{4\pi} \iint_{S_0} \frac{\|\bar{\mathbf{I}}_a(\omega) - \tilde{\mathbf{I}}_o(\omega)\|}{\|\bar{\mathbf{I}}_a(\omega)\|} dS_0 \right], \quad (31)$$

where $\tilde{\mathbf{I}}_o(\omega)$ is the intensity measured using the array with mismatched components.

The low frequency bound, f_{LO} , above which the array has an acceptable accuracy, is defined in this article as the frequency at which $\forall(\theta, \phi, f < f_{LO}) : \chi(\theta, \phi, \omega) \geq -10$ dB. The high frequency bound, f_{HI} , below which the array has an acceptable accuracy, is defined in this article as the highest frequency at which $\forall(\theta, \phi, f > f_{HI}) : \chi(\theta, \phi, \omega) \geq -10$ dB. The *measurement bandwidth* is defined as $f_{BW} = f_{HI} - f_{LO}$.

In the following section, only the phase differences between individual components are investigated as the magnitude responses can be accurately equalized using digital filters to obtain magnitude matched components at lower frequencies (e.g. by using frequency warped filters [32][33]), but the phase mismatches are harder to correct.

C. Numerical comparison

Four different aspects of the proposed arrays are numerically assessed in this section. These are 1) the far-field performance, 2) the near-field performance, 3) the effects of array size, and 4) the measurement bandwidth. In the following discussion, the arrays with 4, 12 and 20 elements use the finite element quadrature, the arrays with 6, 14 and 26 elements use the Lebedev quadrature, and the arrays with 8, 18 and 32 elements use the product Gauss quadrature for calculating the particle velocity. For conciseness, these arrays will be referred to

as KH-FEQ4, KH-FEQ12, KH-FEQ20, KH-LQ6, KH-LQ14, KH-LQ26, KH-PGQ8, KH-LQ18, KH-PGQ32, respectively. It should be noted that the acoustic free-field conditions are assumed in the simulations given in this section. Note also that the reported values are not exact due to the finite resolution of the frequency and the source directions used in the simulations.

1) *Far-field performance*: The accuracy of the proposed array topologies was assessed by simulating a monochromatic point source positioned 10 m away from the arrays. This way, the performance of the proposed arrays was quantified for predominantly active sound fields. In all of the simulated cases the array radius was selected as 3 cm. The individual elements of the arrays were assumed to be perfectly matched, representing the ideal case scenario.

Fig. 7 shows the directional errors for the proposed array topologies up to 3 kHz. This frequency is slightly higher than the maximum frequency ($f = 2.8$ kHz) for which the finite difference approximation in (16) holds. The white contour lines, where shown, represent the regions within which the directional error is less than 1° . The arrays with fewer than 12 elements (e.g. KH-FEQ4, KH-LQ6, and KH-PGQ8) have a strongly direction dependent accuracy with errors up to 8.3° . Arrays with 12 or more elements (e.g. KH-FEQ12, KH-LQ14, KH-LQ18, KH-FEQ20, KH-LQ26, and KH-PGQ32) achieve a significantly higher accuracy with less than 1° directional error for all simulated source frequencies. In all cases, the directional error is minimum along the directions of the individual components as well as their pairwise average directions.

Fig. 8 shows the magnitude error in the horizontal plane for different spherical array topologies up to 3 kHz. The black contour lines show the region within which the magnitude error is less than -10 dB. It may be observed that for the array topologies having fewer than 12 elements the magnitude error is not distributed uniformly and can be as high as -5 dB for some directions. Such a strong dependence of accuracy on the source direction is not desirable. In contrast, arrays with 12 or more elements will achieve a very uniform distribution of magnitude error. In all cases, the magnitude error is maximum along the directions of the individual components.

Fig. 9 shows the isotropic operating ranges (f_{IOR}) of different array topologies for a maximum directional error of 1° and a maximum magnitude error of -10 , -15 , and -20 dB, respectively. If a magnitude error of -10 dB can be tolerated, an operating range of up to 2.5 kHz can be achieved with the arrays having 12 or more elements. Increasing the number of array elements increases the directional accuracy but not the magnitude accuracy. Since the isotropic operating range is defined based on both the magnitude and the directional errors, the operating range never exceeds 2.5 kHz. This indicates that, with the given definition of isotropic operating range, the best trade-off between the far-field operating range and the element count is achieved by the KH-FEQ12 array.

2) *Near-field performance*: The pressure and the particle velocity components of the sound field due to a point source in the acoustic near-field are out of phase. Such a sound field has both active and reactive components. In order to quantify the performance of the proposed arrays in the near-field of a

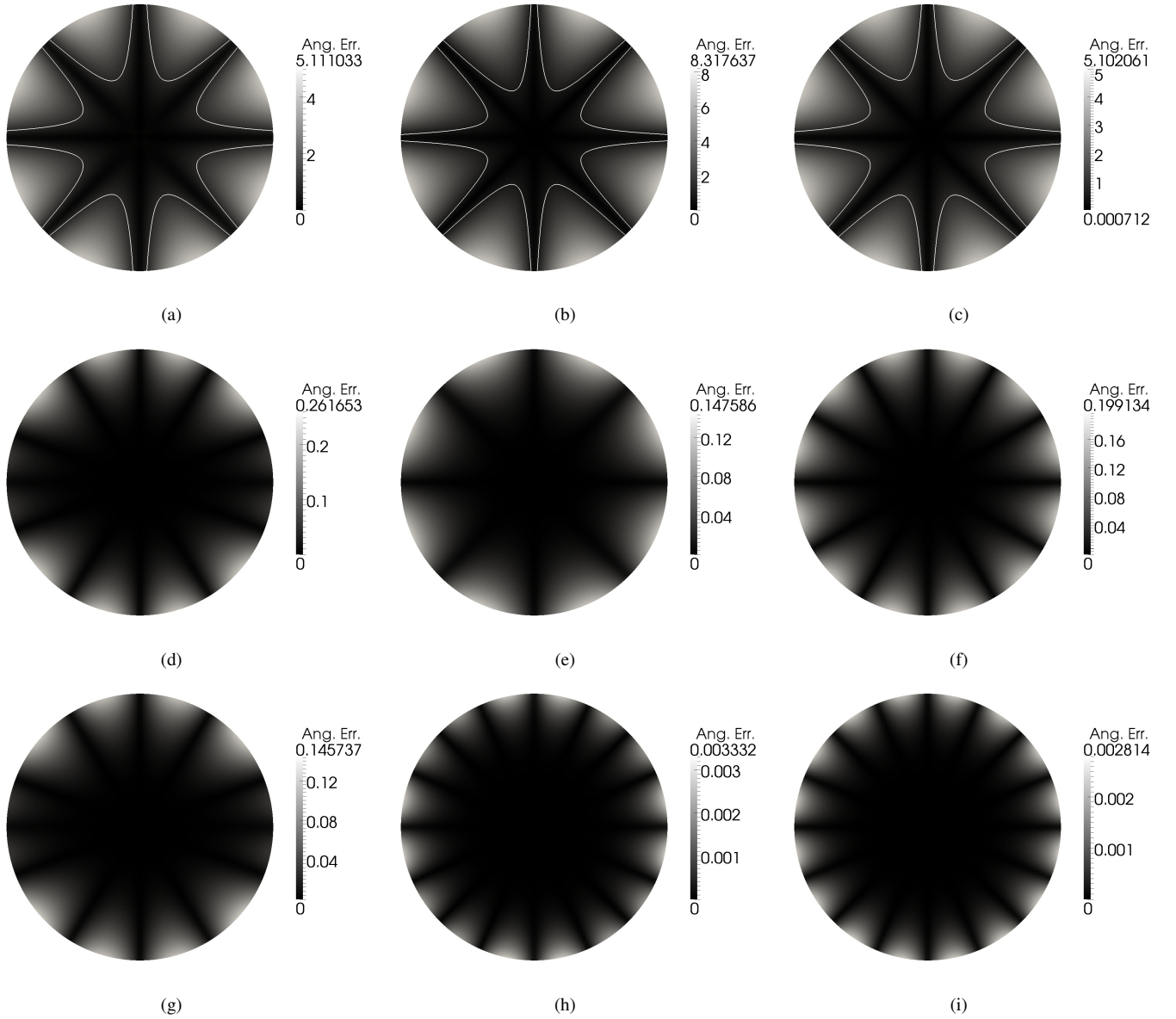


Fig. 7. Directional errors in the horizontal plane for a monochromatic point source positioned at 10 m, for the (a) KH-FEQ4, (b) KH-LQ6, (c) KH-PGQ8, (d) KH-FEQ12, (e) KH-LQ14 (f) KH-LQ18, (g) KH-FEQ20, (h) KH-LQ26, and (i) KH-PGQ32 arrays. The radial axes which represent the frequency are linearly scaled. The center of each disk represents zero frequency, and the outer edge represents 3 kHz. Top, left, bottom and right of each disk represent 0 , $\pi/2$, π , $3\pi/2$ azimuth directions, respectively. The region within the white contour (where shown) represents the directional errors less than 1° .

source, a point source at 10 cm distance from the arrays with $R = 3$ cm was simulated. The accuracy of KH-FEQ4, KH-LQ6, and KH-PGQ8 arrays are severely impaired either due to magnitude errors or due to directional errors. The accuracy of these arrays for the near-field source are even more strongly direction dependent at low frequencies for which the effects of near-field are stronger.

Descriptive statistics of the magnitude and directional errors of different array topologies for frequencies up to 3 kHz are given in Table I. It may be observed that all the arrays with 12 or more elements achieve a good accuracy with the maximum error only slightly higher than -10 dB. As with the far-field case, KH-FEQ12 array achieves the best trade-off between the number of elements and the accuracy in near-field.

3) *Array radius*: Due to the implicit use of finite difference approximations for calculating the particle velocity, the array radius has a significant effect on the operating range of the probe. This effect was investigated by simulating arrays with radii between 2 cm and 10 cm for a point source positioned at 10 m distance. Fig. 10 shows the isotropic operating ranges, f_{IOR} , for different array radii. It may be observed that decreasing the array radius increases the operating range as expected. It must be noted however that physical limitations due to finite microphone size would prevent designing arrays with very small radii. The operating ranges follow a similar overall trend for different array sizes, but KH-FEQ12 array provides the best trade-off between the operating range and the number of elements.

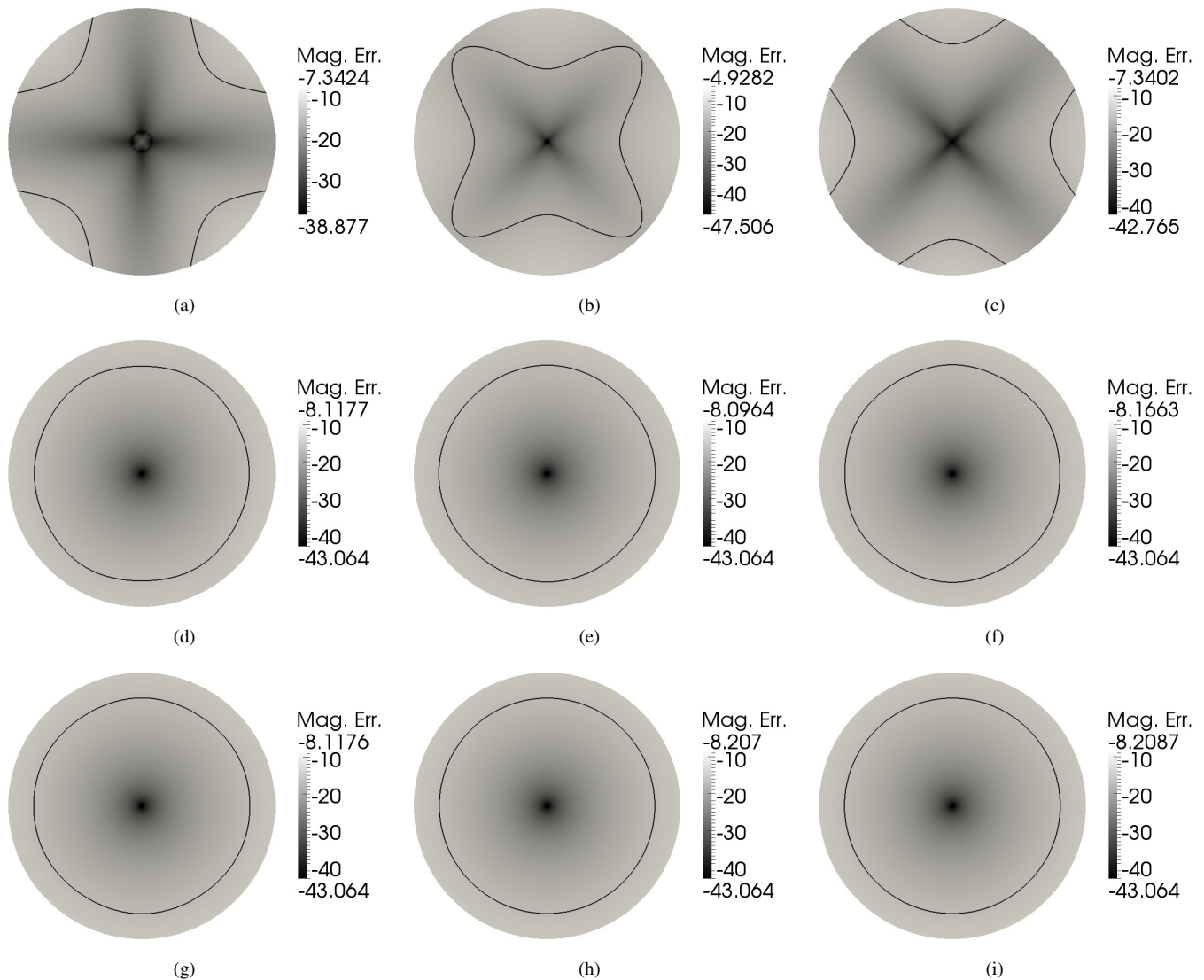


Fig. 8. Magnitude errors in the horizontal plane for a monochromatic point source positioned at 10 m, for the (a) KH-FEQ4, (b) KH-LQ6, (c) KH-PGQ8, (d) KH-FEQ12, (e) KH-LQ14 (f) KH-LQ18, (g) KH-FEQ20, (h) KH-LQ26, and (i) KH-PGQ32 arrays. The radial axes which represent the frequency are linearly scaled. The center of each disk represents zero frequency, and the outer edge represents 3 kHz. Top, left, bottom and right of each disk represent 0 , $\pi/2$, π , $3\pi/2$ azimuth directions, respectively. The region within the black contour represents the magnitude errors less than -10 dB.

4) *Measurement bandwidth*: The robustness of the proposed arrays for phase mismatches is evaluated and the low and high frequency bounds as well as the measurement bandwidths for each array topology are numerically obtained in this section.

Three cases are investigated: In the first case, phase mismatches are simulated for the KH-FEQ12 array ($R = 3$ cm) by applying a random, frequency-independent phase mismatch to each component. The phase discrepancies come from normal distributions with zero mean and the standard deviations of 0.2° , 0.3° , 0.4° , and 0.5° . In the second case, the array radii of 2, 4, 6, 8 and 10 cm are simulated for the KH-FEQ12 array and for a phase mismatch standard deviation of 0.3° . In the third case, all proposed array topologies are compared with respect to their bandwidths for an array radius of 3 cm and

a phase mismatch with a standard deviation of 0.4° ¹. In all cases, monochromatic plane wave fields in different directions around the array are simulated. Azimuth resolution is 6° and elevation resolution is 12° . The reported values are based on the maximum direction averaged error norms observed for all simulated directions.

Fig. 11 shows the direction averaged error norms for the KH-FEQ12 array for a fixed array radius of 3 cm with different levels of phase mismatch. The error for the perfectly matched case is also shown for comparison². The circles on each error curve represent the low frequency bounds for the respective

¹The simulated phase mismatches correspond to high levels of variation, especially at low frequencies. Individual components of state-of-the-art intensity probes typically have a maximum phase mismatch of 0.05° below 250 Hz [13].

²Observe that the error curve for the perfectly matched array is monotonically increasing, and that the perfectly matched array does not have a low frequency bound.

TABLE I
DESCRIPTIVE STATISTICS OF THE MAGNITUDE ERRORS (IN DB) FOR A SOURCE IN THE ACOUSTIC NEAR FIELD ($R_m = 10$ CM)

Array Type	ϵ_{\max} (dB)	$\bar{\epsilon}$ (dB)	stdev $[\epsilon]$ (dB)	ψ_{\max}	$\bar{\psi}$	stddev $[\psi]$
KH-FEQ4	-4.30	-10.05	4.24	14.67	9.36	2.94
KH-LQ6	-5.95	-9.48	2.37	3.33	1.80	0.70
KH-PGQ8	-11.73	-17.42	4.48	2.21	1.13	0.43
KH-FEQ12	-9.74	-12.41	2.85	0.19	0.07	0.05
KH-LQ14	-9.81	-12.42	2.84	0.18	0.05	0.04
KH-PGQ18	-9.81	-12.39	2.83	0.16	0.05	0.03
KH-FEQ20	-9.90	-12.43	2.87	0.11	0.04	0.03
KH-LQ26	-9.96	-12.44	2.83	0.01	2×10^{-3}	2×10^{-3}
KH-PGQ32	-9.96	-12.44	2.82	0.01	2×10^{-3}	2×10^{-3}

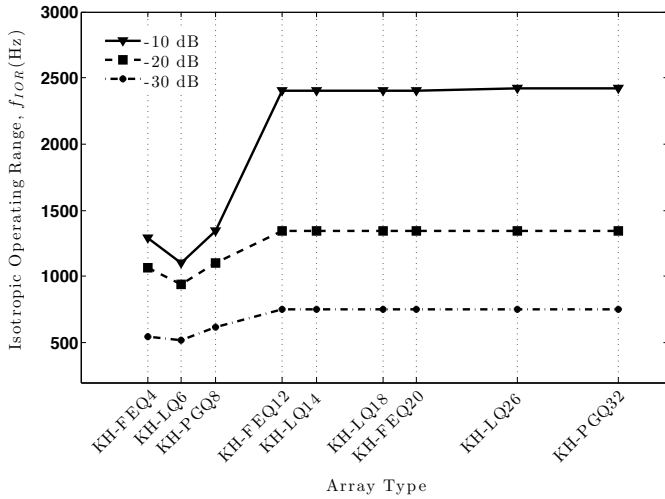


Fig. 9. Isotropic operating ranges for different array topologies with $R = 3$ cm and for different magnitude error bounds. The simulated point source is positioned at $R_s = 10$ m.

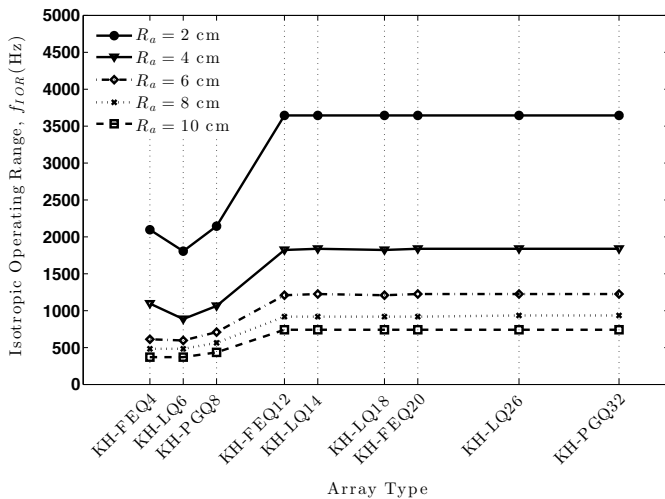


Fig. 10. Isotropic operating ranges for different array topologies (with -10 dB magnitude error and 1° directional error bound) and for different array radii. The simulated point source is positioned at $R_s = 10$ m.

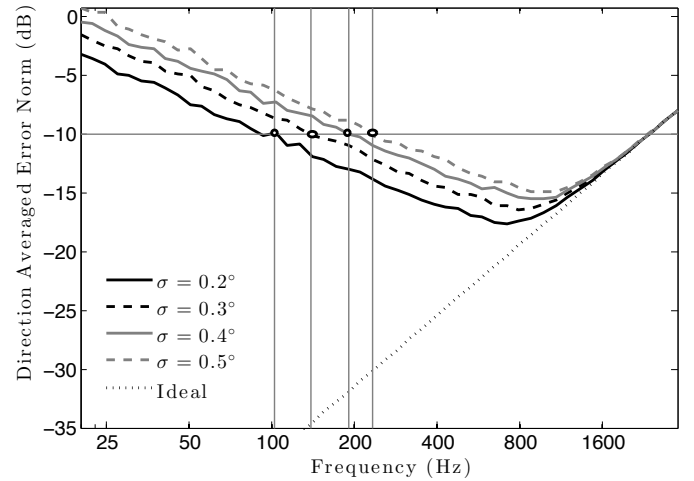


Fig. 11. Maximum direction averaged error norms and the low frequency bounds for the KH-FEQ12 array for different levels of phase mismatch between components. The array radius is $R = 3$ cm. The low frequency bound for each level of phase mismatch is shown by a small circle. The error for the perfectly matched case is also shown for comparison.

case where the direction averaged error norm is less than -10 dB. It may be observed that the main degrading effect of the phase mismatches occurs at low frequencies. The error and the lower frequency bound increase with the level of phase mismatch, while the accuracy at higher frequencies converge to that of the ideal case and are not significantly affected. The low and high frequency bounds as well as the measurement bandwidths are given in Table II.

Fig. 12 shows the direction averaged error norms for the KH-FEQ12 array with different radii with a phase mismatch having a standard deviation of 0.4° . It may be observed that the low and high frequency bounds as well as the measurement bandwidth are inversely proportional to array radius. The choice of the array radius is thus a matter of choosing the frequency range of interest. The low and high frequency bounds as well as the measurement bandwidths are given in Table II.

Finally, different array topologies with a common radius of 3 cm and a phase mismatch standard deviation of 0.4° are simulated. The results indicate that a significant gain over an

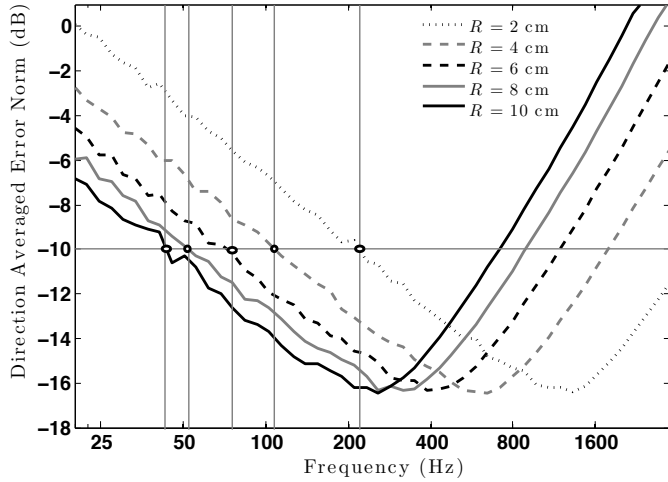


Fig. 12. Maximum direction averaged error norms and the low frequency bounds for the KH-FEQ12 array for different array radii and for a phase mismatch with a standard deviation of 0.4° . The low frequency bound for each level of phase mismatch is shown by a small circle.

8-element array (KH-PGQ8) can be achieved by using a 12-element array (KH-FEQ12). Among all the simulated array topologies, the KH-FEQ12 array provides the best trade-off between the element count and the achieved measurement bandwidth. Although a slightly better low frequency accuracy can be achieved, the additional bandwidth gain is not significant for the arrays with greater number of elements. Table II summarizes the low and high frequency bounds as well as the bandwidths for these cases.

TABLE II
LOW AND HIGH FREQUENCY BOUNDS (f_{LO} AND f_{HI}) AND MEASUREMENT BANDWIDTHS (f_{BW}) OF THE PROPOSED ARRAY TOPOLOGIES.

Array Type	R (cm)	Phase mismatch	f_{LO} (Hz)	f_{HI} (Hz)	f_{BW} (Hz)
KH-FEQ4	3	0.4°	347	1231	884
KH-LQ6	3	0.4°	281	1116	835
KH-PGQ8	3	0.4°	247	1224	977
KH-FEQ12	2	0.4°	221	3560	3339
		0.2°	102	2375	2273
		0.3°	109	2375	2266
		0.4°	183	2375	2192
		0.5°	232	2375	2143
	4	0.4°	107	1799	1692
	6	0.4°	76	1195	1119
	8	0.4°	52	905	853
10	0.4°	43	716	673	
KH-LQ14	3	0.4°	169	2384	2215
KH-PGQ18	3	0.4°	150	2382	2232
KH-FEQ20	3	0.4°	137	2392	2255
KH-LQ26	3	0.4°	119	2403	2284
KH-PGQ32	3	0.4°	118	2405	2287

5) *Comparison with conventional arrays*: Three types of conventional arrays are discussed and compared with the KH-FEQ12 array in this section. The first type is the tetrahedral array embodying four pressure probes [34]. An example to this type of an array is the *Ono-Sokki Tetra-phone*. The second type is an octahedral array which embodies six pressure probes [35]. A commercially available example is the *G.R.A.S. Vector Intensity Probe Type 50VI* [36]. The third type is a class of array designs based on a least-squares formulation and embodies first-order directional microphones [37].

a) *Ono-Sokki Tetra-phone*: This array is composed of four pressure microphones positioned at the vertices of a tetrahedron [34][16][38]. The pressure at the center is approximated as the average of the pressure signals recorded by these microphones such that:

$$p_o(\omega) = \frac{1}{4} \sum_{k=1}^4 p_k(\omega) \quad (32)$$

where $p_k(\omega) = p(\mathbf{x}_k, \omega)$ and \mathbf{x}_k is the k^{th} vertex of the tetrahedron. The particle velocity components at the directions of the vertices are given as:

$$\mathbf{v}_k(\omega) = -(p_k(\omega) - p_o(\omega)) / (j\omega\rho_0 R). \quad (33)$$

These approximations correspond not to the actual particle velocity at the center but at three different points $R/2$ away from the center.

The particle velocity components in the axial directions are calculated as [16]

$$\begin{aligned} \mathbf{v}_x(\omega) &= -\frac{\sqrt{3}}{2\sqrt{2}} (\mathbf{v}_2(\omega) - \mathbf{v}_3(\omega)) \\ \mathbf{v}_y(\omega) &= -\frac{1}{2\sqrt{2}} (2\mathbf{v}_1(\omega) - \mathbf{v}_2(\omega) - \mathbf{v}_3(\omega)) \\ \mathbf{v}_z(\omega) &= -\frac{1}{4} (\mathbf{v}_1(\omega) + \mathbf{v}_2(\omega) + \mathbf{v}_3(\omega) - 3\mathbf{v}_4(\omega)). \end{aligned} \quad (34)$$

After obtaining the particle velocity vector, the time-averaged acoustic intensity can be calculated using (28).

b) *G.R.A.S. Type 50VI*: These arrays have octahedral topology and embody three p - p pairs positioned along the three orthogonal axes [36]. The particle velocity along each axial direction is calculated using the finite-difference approximation given in (16). The pressure at the center is calculated as the average of the pressure signals from the six individual pressure probes. *Brüel & Kjaer Type 5356* also has the same topology and uses a similar finite-difference approach [35].

c) *Least-squares based (LS) arrays*: Least-squares based arrays [37] embody first-order directional microphones positioned at diametrically opposite points on an open sphere with their acoustic axes facing radially outwards. An omnidirectional microphone at the center is used to measure the actual pressure. The assumptions are made that the source is in the acoustic far-field and that the array radius is much smaller than the quarter wavelength. If all the microphones have the ideal first-order directivity function, $\Gamma(\theta) = (1 - \alpha) + \alpha \cos \theta$ and are facing radially outwards, the acoustic intensity can be

calculated as:

$$\mathbf{I}_o(\omega) \approx \frac{3p_o(\omega)}{2\rho_0 c K \alpha} \sum_{k=1}^K p_{k,\alpha}(\omega) \mathbf{n}_k, \quad (35)$$

where $p_{k,\alpha}(\omega)$ is the signal recorded by the k^{th} first-order directional microphone, $p_o(\omega)$ is the pressure at the center, \mathbf{n}_k is the unit vector from the position of the k^{th} microphone to the center, and K is the total number of microphones on the open sphere. It may be observed from (35) that the predicted intensity is not a function of array radius. This desirable property is maintained as long as the array radius is less than the quarter wavelength. This means that the least-squares based arrays are subject to the same constraints as the other arrays at high frequencies but they are not significantly affected at low frequencies by component mismatches.

While it is possible to have an arbitrary distribution of microphone pairs as long as they are positioned at diametrically opposite points, regular polyhedra (i.e. octahedral, cubic, icosahedral, and dodecahedral topologies) are preferred in order to achieve a spherically symmetric distribution of directional and magnitude errors. The individual elements can have any first-order directivity. The octahedral LS array topology with cardioid microphones was previously employed for recording sound fields for the purpose of loudspeaker-based auralization [39]. An ideal cardioid directivity is also employed in the simulations in the following section.

d) *Measurement bandwidths of conventional arrays:* In order to compare the proposed arrays with the conventional arrays described above, a fixed array radius of 3 cm is chosen. Monochromatic plane waves incident from all directions around the arrays were simulated. The azimuth and elevation resolution were 6° and 12° , respectively. A comparison of two widely used conventional arrays (*Ono-Sokki Tetra-probe* and *G.R.A.S. Type 50VI*), four least-squares (LS) arrays with the proposed KH-FEQ12 array is given. Phase mismatches are obtained from a normal distribution with a standard deviation of 0.4°

The low and the high frequency bounds as well as measurement bandwidths for a maximum direction averaged error norm of -10 dB are given in Table III. All of the simulated conventional arrays have lower bandwidths and perform poorly in comparison with the KH-FEQ12 array. It may be observed that the KH-FEQ12 array has a bandwidth more than twice as high as the LS array with the same number of elements. The major advantage of LS arrays is their accuracy at low frequencies which does not suffer significantly from phase mismatches. The higher bandwidth achieved by the KH-FEQ12 array is mainly due to the fact that the finite difference approximation to particle velocity is obtained using pressure probes separated by R as opposed to $2R$ in the LS arrays.

V. DISCUSSION AND CONCLUSIONS

Spherical microphone arrays can be used to measure the acoustic intensity in 3-D. This article presented a theoretical analysis of such arrays in terms of their performance in the acoustic far- and near-fields, size, and measurement bandwidth.

TABLE III
LOW AND HIGH FREQUENCY BOUNDS (f_{LO} AND f_{HI}) AND MEASUREMENT BANDWIDTHS (f_{BW}) OF PHASE-MISMATCHED CONVENTIONAL 3-D ACOUSTIC INTENSITY PROBES IN A PLANE WAVE FIELD.

Array type	Element count	f_{LO} (Hz)	f_{HI} (Hz)	f_{BW} (Hz)
Ono-Sokki [34][16][38]	4	380	984	596
G.R.A.S. Type 50VI [36]	6	284	910	626
Octahedral (LS) [39][37]	6 + 1	d.c.	638	638
Cubic (LS) [37]	8 + 1	d.c.	752	752
Icosahedral (LS) [37]	12 + 1	d.c.	1048	1048
Dodecahedral (LS) [37]	20 + 1	d.c.	1051	1051
Icosahedral (KH-FEQ12)	12 + 1	183	2375	2192

First, the calculation of the particle velocity was formulated using the Kirchhoff-Helmholtz integral on an open spherical surface. Then, the formulation was simplified for the condition where the pressure is known at the center of the open sphere. Numerical quadrature schemes to obtain an approximation to the particle velocity at the center were discussed and the corresponding array topologies were presented. These array topologies were then numerically evaluated for their accuracy, operating range, effects of the array radius, and component mismatches.

The main findings are as follows:

- 1) The directional dependence of the error is very prominent for the array topologies with fewer than 12 elements. This dependence was not observed for the array topologies with 12 or more elements.
- 2) The isotropic operating range was defined for perfectly matched arrays as the highest frequency for which the magnitude and directional errors are both uniformly less than given magnitude and angle thresholds. It was observed that a good accuracy with at most -10 dB magnitude error and at most 1° directional error is possible up to around 2.5 kHz for an array radius of 3 cm for arrays with 12 or more elements. Isotropic operating range was observed to be inversely proportional to array radius.
- 3) The effects of phase mismatches between array elements were numerically investigated. The direction averaged error norm was defined as the norm of the difference vector between the actual intensity and the intensity measurement obtained from a phase mismatched array. The measurement bandwidth was defined as the frequency range where this error is less than -10 dB. Numerical simulations with small phase mismatches on individual array elements were carried out. It was observed that phase mismatches impair the accuracy of the array at low frequencies while the accuracy at high frequencies is not significantly affected. The best trade-off between the number of microphones and the measurement bandwidth was achieved by the 12-element array. Arrays with more than 12 elements provided only

minor improvements.

- 4) A numerical comparison with conventional arrays revealed that the proposed arrays increased the measurement bandwidth of intensity measurements by a factor of two.

ACKNOWLEDGMENTS

The author would like to thank Dr Tolga Özkurt and the two anonymous reviewers for their valuable feedback and insightful comments.

REFERENCES

- [1] F. Fahy, *Sound intensity*, 2nd ed. E & FN Spon Press, 1995.
- [2] S. Gade, "Sound intensity, Part I: Theory," *Brüel & Kjaer Tech. Rev.*, vol. 3, pp. 3–39, 1982.
- [3] F. Jacobsen, "A note on instantaneous and time-averaged active and reactive sound intensity," *Journal of Sound and Vibration*, vol. 147, no. 3, pp. 489–496, 1991.
- [4] R. Hickling, W. Wei, and R. Raspet, "Finding the direction of a sound source using a vector sound-intensity probe," *J. Acoust. Soc. Am.*, vol. 94, no. 4, pp. 2408–2412, 1993.
- [5] S. Tervo, "Direction estimation based on sound intensity vectors," in *Proc. of European Signal Process. Conf. (EUSIPCO 2009)*, 2009, pp. 700–704.
- [6] B. Günel and H. Hacıhabiboğlu, "Sound source localization: Conventional methods and intensity vector direction exploitation," in *Machine Audition: Principles, Algorithms and Systems*, W. Weng, Ed. Hershey, PA: IGI Global, 2011.
- [7] B. Günel, H. Hacıhabiboğlu, and A. Kondoç, "Acoustic source separation of convolutive mixtures based on intensity vector statistics," *IEEE Trans. Audio, Speech, Lang. Process.*, vol. 16, no. 4, pp. 748–756, May 2008.
- [8] —, "Intensity vector direction exploitation for exhaustive blind source separation of convolutive mixtures," in *Proc. 2009 IEEE Int. Conf. Acoust. Speech and Signal Process., (ICASSP 2009)*, april 2009, pp. 41–44.
- [9] X. Chen, A. Alinaghi, X. Zhong, and W. Wang, "Acoustic vector sensor based speech source separation with mixed gaussian-laplacian distributions," in *Proc. 18th Int. Conf. on Digital Signal Process. (DSP 2013)*, Santorini, Greece, 1-3 July 2013.
- [10] J. Vilkamo, T. Lokki, and V. Pulkki, "Directional audio coding: Virtual microphone-based synthesis and subjective evaluation," *J. Audio Eng. Soc.*, vol. 57, no. 9, pp. 709–724, September 2009.
- [11] I. Elfritri, B. Günel, and A. M. Kondoç, "Multichannel audio coding based on analysis by synthesis," *Proc. of IEEE*, vol. 99, no. 4, pp. 657–670, April 2011.
- [12] F. Jacobsen and H.-E. de Bree, "A comparison of two different sound intensity measurement principles," *J. Acoust. Soc. Am.*, vol. 118, no. 3, pp. 1510–1517, September 2005.
- [13] F. Jacobsen, "Sound intensity," in *Springer Handbook of Acoustics*, 1st ed. Springer Verlag, 2007, pp. 1053–1075.
- [14] H.-E. de Bree, W. Druyvesteyn, E. Berenschot, and M. Elwenspoek, "Three-dimensional sound intensity measurements using microflowed particle velocity sensors," in *Twelfth IEEE Int. Conf. on Micro Electro Mech. Syst. (MEMS '99)*, jan 1999, pp. 124–129.
- [15] R. Raangs, F. Druyvesteyn, and H.-E. de Bree, "A low-cost intensity probe," *J. Audio Eng. Soc.*, vol. 51, no. 5, pp. 344–367, May 2003.
- [16] H. Suzuki, S. Oguro, M. Anzai, and T. Ono, "Performance evaluation of a three dimensional intensity probe," *J. Acoust. Soc. Jpn.*, vol. 16, no. 4, pp. 233–238, 1995.
- [17] B. S. Cazzolato and C. H. Hansen, "Errors arising from three-dimensional energy density sensing in one-dimensional sound fields," *J. Sound Vib.*, vol. 236, no. 3, pp. 375–400, 2000.
- [18] G. Moschioni, B. Saggini, and M. Tarabini, "3-D sound intensity measurements: Accuracy enhancements with virtual-instrument-based technology," *IEEE Trans. Instr. Meas.*, vol. 57, no. 9, pp. 1820–1829, Sept. 2008.
- [19] F. Jacobsen and E. S. Olsen, "Testing sound intensity probes in interference fields," *Acta Acustica united with Acustica*, vol. 80, no. 2, pp. 115–126, 1994.
- [20] S. Gade, "Sound intensity, Part II: Instrumentation & applications," *Brüel & Kjaer Tech. Rev.*, vol. 4, pp. 3–32, 1982.
- [21] A. D. Pierce, *Acoustics: An introduction to its physical principles and applications*. Woodbury, NY, USA: Acoustical Society of America, 1994.
- [22] E. G. Williams, *Fourier Acoustics: Sound radiation and nearfield acoustic holography*. Academic Press, 1999.
- [23] F. Fahy, *Foundations of Engineering Acoustics*. Academic Press, 2001.
- [24] V. Lebedev and D. Laikov, "A quadrature formula for the sphere of the 131st algebraic order of accuracy," *Doklady Math.*, vol. 59, no. 3, pp. 477–481, 1999.
- [25] K. Atkinson, "Numerical integration on the sphere," *J. Austral. Math. Soc. (Series B)*, vol. 23, pp. 332–347, 1982.
- [26] F. Fahy, "International standards for the determination of sound power levels of sources using sound intensity measurement: an exposition," *Appl. Acoust.*, vol. 50, no. 2, pp. 97–109, 1997.
- [27] I. Tashev, "Beamformer sensitivity to microphone manufacturing tolerances," in *19th Int. Conf. Systems for Automation of Engineering and Research (SAER 2005)*, 2005.
- [28] G. Krishnappa, "Cross-spectral method of measuring acoustic intensity by correcting phase and gain mismatch errors by microphone calibration," *J. Acoust. Soc. Am.*, vol. 69, no. 1, pp. 307–310, 1981.
- [29] F. Jacobsen, "An overview of the sources of error in sound power determination using the intensity technique," *Appl. Acoust.*, vol. 50, no. 2, pp. 155–166, 1997.
- [30] —, "A note on finite difference estimation of acoustic particle velocity," *J. Sound Vib.*, vol. 256, no. 5, pp. 849–859, 2002.
- [31] J. Y. Chung, "Cross-spectral method of measuring acoustic intensity without error caused by instrument phase mismatch," *J. Acoust. Soc. Am.*, vol. 64, no. 6, pp. 1613–1616, December 1978.
- [32] M. Karjalainen, A. Härmä, U. Laine, and J. Huopaniemi, "Warped filters and their audio applications," in *Proc. 1997 IEEE Workshop on Applications of Signal Processing to Audio and Acoustics (WASPAA'97)*, 1997.
- [33] A. Härmä, M. Karjalainen, L. Savioja, V. Välimäki, U. K. Laine, and J. Huopaniemi, "Frequency-warped signal processing for audio applications," *J. Audio Eng. Soc.*, vol. 48, no. 11, pp. 1011–1031, 2000.
- [34] S. Oguro, M. Anzai, H. Suzuki, and T. Ono, "A three-dimensional sound intensity probe," *The Journal of the Acoustical Society of America*, vol. 91, no. 4, pp. 2370–2370, 1992.
- [35] K. H. Miah, "Three-dimensional broadband intensity probe for measuring acoustical parameters," Ph.D. dissertation, The University of Texas at Austin, August 2009.
- [36] *Vector intensity probe Type 50VI-1, Rev. 19*, G.R.A.S. Sound & Vibration, 2006.
- [37] H. Hacıhabiboğlu, "On the accuracy of open spherical microphone arrays for measuring acoustic intensity," in *Proc. 2013 IEEE Workshop on Applications of Signal Processing to Audio and Acoustics (WASPAA'13)*, New Paltz, NY, October 20-23 2013.
- [38] T. Iino, H. Tatekawa, H. Mizukawa, and H. Suzuki, "Numerical evaluation of three-dimensional sound intensity measurement accuracies and a proposal for an error correction method," *Acoust. Sci. Tech.*, vol. 34, no. 1, pp. 34–41, 2013.
- [39] S. Yokoyama, K. Ueno, S. Sakamoto, and H. Tachibana, "6-channel recording/reproduction system for 3-dimensional auralization of sound fields," *Acoust. Sci. Tech.*, vol. 23, no. 2, pp. 97–103, 2002.



Hüseyin Hacıhabiboğlu (S'96-M'00-SM'12) received the B.Sc. (honors) degree from the Middle East Technical University (METU), Ankara, Turkey, in 2000, the M.Sc. degree from the University of Bristol, Bristol, U.K., in 2001, both in electrical and electronic engineering, and the Ph.D. degree in computer science from Queen's University Belfast, Belfast, U.K., in 2004. He held research positions at University of Surrey, Guildford, U.K. (2004-2008) and King's College London, London, U.K. (2008-2011). Currently, he is an Assistant Professor and

Head of Department of Modelling and Simulation at Graduate School of Informatics, Middle East Technical University, Ankara, Turkey. His research interests include audio signal processing, room acoustics, multichannel audio systems, psychoacoustics of spatial hearing, microphone arrays, and game audio. Dr. Hacıhabiboğlu is a member of the IEEE Signal Processing Society, Audio Engineering Society (AES), Turkish Acoustics Society (TAD), and the European Acoustics Association (EAA).